

A transmission electron microscopy study of defects formed through the capping layer of self-assembled InAs/GaAs quantum dot samples

K. Sears,^{a)} J. Wong-Leung, H. H. Tan, and C. Jagadish

Department of Electronic Materials Engineering, Research School of Physical Sciences and Engineering, Australian National University, Canberra, ACT 0200, Australia

(Received 9 August 2005; accepted 22 March 2006; published online 1 June 2006)

Plan-view and cross-sectional transmission electron microscopy have been used for a detailed study of the defects formed in capped InAs/GaAs quantum dot (QD) samples. Three main types of defects, V-shaped defects, single stacking faults, and stacking fault pyramids, were found to form under growth conditions that led to either very large, indium enriched, or coalesced islands. All three types of defects originate at the buried quantum dot layer and then travel through the GaAs cap to the surface on the $\{111\}$ planes. The V-shaped defects were the most common and typically consisted of two pairs of closely spaced 60° Shockley partials with a $\langle 211 \rangle$ line direction. The two pairs originate together at the buried QD layer and then travel in “opposite” directions on different $\{111\}$ planes. The second type of defect is the single stacking fault which consists of a single pair of partial dislocations separated by an ≈ 50 nm wide stacking fault. Finally, both complete and incomplete stacking fault pyramids were observed. In the case of the complete stacking fault pyramid the bounding dislocations along the $[110]$, $[1\bar{1}0]$, $[10\bar{1}]$, and $[101]$ directions were identified as stair rods. A possible mechanism for the stacking fault pyramid formation, which can also account for the creation of incomplete stacking fault pyramids, is presented. © 2006 American Institute of Physics. [DOI: [10.1063/1.2197038](https://doi.org/10.1063/1.2197038)]

I. INTRODUCTION

The self-assembled growth of quantum dots (QDs) via the Stranski-Krastanow growth mode has attracted great interest due to its potential for improved optoelectronic devices. In the Stranski-Krastanow mode, strain accumulation due to lattice mismatch drives the formation of three-dimensional (3D) islands after a certain planar critical thickness is reached. For InAs/GaAs where the lattice mismatch is high ($\approx 7.2\%$), coherent/defect-free islands begin to form after only ≈ 1.7 ML (monolayer) of InAs. However, if the growth parameters are not controlled tightly, and the islands allowed to grow too large or coalesce, the same strain that drives island formation also leads to defect nucleation. Such defects need to be avoided in order to achieve reliable high performance devices. This is particularly an issue for growth of InAs/GaAs QDs by metal organic chemical vapor deposition (MOCVD), where there is an increased tendency for the islands to coalesce.

The elastic strain relaxation and defect generation are very different in the case of epitaxial growth via island nucleation. Dislocations tend to nucleate at the island edges which are areas of higher strain and at the overlapped region between two coalesced islands,^{1–3} and can then thread through to the surface. This means that the arrays of orthogonal interfacial dislocations which are typical of two-dimensional (2D) growth do not tend to form and are instead replaced by a number of interesting defect structures. For example, Chu *et al.*⁴ report on pyramidal dislocation tangles

formed due to activation of the four $\{111\}$ planes above interfacial misfit particles with a number of dislocations threading to the surface. Grown in stacking fault structures such as double triangular stacking fault pairs, stacking fault pyramids and trapezoids, originating close to the interface, have been reported by many groups for ZnSe grown on GaAs and were attributed to a combination of the starting surface reconstruction and island formation during the initial stages of growth.^{5–8}

While there have been quite a few studies of defects formed in freestanding, uncapped QDs grown in the Stranski-Krastanow growth mode,^{1,2,9,10} there seems to be relatively few studies of the defects generated during capping of the QDs.^{11–13} However, for most device applications, these islands must be capped with a material of wider band gap (e.g., a GaAs cap in the case of InAs/GaAs QDs) in order to achieve the beneficial 3D confinement effects. During an extensive study of the various growth parameters¹⁴ on InAs/GaAs QD nucleation, three main defect types were observed under certain growth conditions. These defects thread through the GaAs capping layer and are similar to those reported by Ueda *et al.*¹¹ In this paper we present a detailed transmission electron microscopy (TEM) analysis of these defects and their possible formation mechanisms.

II. EXPERIMENT

The InAs/GaAs QD samples were grown on (100) semi-insulating (SI) GaAs by low-pressure (100 mbar) MOCVD. The basic structure is shown in Fig. 1 and consists of both a buried QD layer and a layer of QDs on the surface. In this

^{a)}Electronic mail: kks109@rsphysse.anu.edu.au

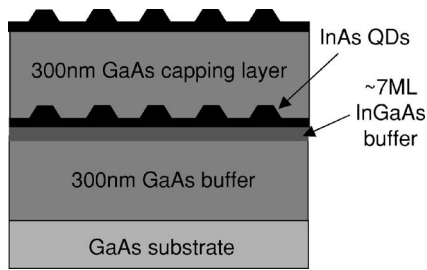


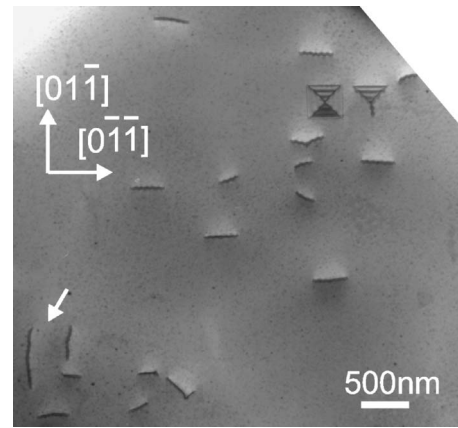
FIG. 1. Schematic showing the sample structure.

paper we concentrate on one sample in which the InAs QDs were deposited onto a very thin $\text{In}_{0.15}\text{Ga}_{0.85}\text{As}$ buffer layer. We found that the use of an InGaAs buffer layer led to increased defect densities, possibly due to indium segregation from the InGaAs layer to the islands, leading to indium enriched islands.¹⁵ The islands were formed by depositing nominally 1.5 ML of InAs at a rate of 0.5 ML/s and using a V/III ratio of 40. This InAs coverage gave the optimum QD photoluminescence intensity. It should be noted that the same defects but at much lower concentrations were also observed under certain growth conditions for InAs QDs deposited directly onto GaAs (i.e., with no $\text{In}_{0.15}\text{Ga}_{0.85}\text{As}$ buffer layer). Further details of the growth conditions can be found elsewhere.^{14–16}

The buried QDs were studied extensively using both plan-view and cross-sectional TEM. The surface QDs were etched away prior to plan-view TEM sample preparation, leaving only the buried QDs for imaging. The plan-view TEM samples were prepared by mechanically polishing the samples to 150 μm followed by dimpling to a thickness of 40 μm and chemically etching with $\text{H}_2\text{SO}_4:\text{H}_2\text{O}_2:\text{H}_2\text{O}$ (3:1:1). Some of the micrographs in this paper were taken in very thin regions of the foil, where the chemical etch has also removed the buried QD layer, leaving only the “upper” regions of the capping layer for imaging. Samples for cross-sectional TEM were prepared by gluing together two pieces cleaved from the wafer along one of the $\{011\}$ planes. These were then mechanically polished followed by Ar ion beam thinning to electron transparency. The TEM analysis was carried out using a Philips CM 300 electron microscope instrument operated at 200 kV. For our TEM investigations, the wafer normal is defined as the $[100]$ direction, thus defining the plan-view foil normal as close to the $[100]$ direction and the cross-sectional foil normal as close to one of the two $\langle 011 \rangle$ directions. Detailed diffraction contrast analysis of the three predominant defects was performed to understand their character. The defects were imaged with both \mathbf{g} and reverse \mathbf{g} using a $\mathbf{g}(>3\mathbf{g})$ always with positive deviation. The Burgers vector of the individual defects was determined using the invisibility criteria of $\mathbf{g} \cdot \mathbf{b} = 0$ and $\mathbf{g} \cdot (\mathbf{b} \times \mathbf{u}) \leq 0.64$.¹⁷ True invisibility is defined when the defect is invisible in both $+\mathbf{g}$ and $-\mathbf{g}$ images.

III. RESULTS

High defect densities were observed for QD samples grown under conditions that led to either (a) larger QDs, (b) the coalescence of QDs, or (c) indium enriched QDs. Figure

FIG. 2. Plan-view TEM image taken under on-axis, $[100]$, bright field conditions of InAs QDs deposited onto a nominally 7 ML $\text{In}_{0.15}\text{Ga}_{0.85}\text{As}$ buffer layer.

2 is a plan-view TEM micrograph of the sample studied in detail, in which the InAs QDs were deposited onto a thin $\text{In}_{0.15}\text{Ga}_{0.85}\text{As}$ buffer layer, leading to indium enriched islands.¹⁵ A high defect density of $\approx 1 \times 10^8 \text{ cm}^{-2}$ is clearly present. The observed defects can be categorized into three main defect structures, namely, (a) V-shaped defects, (b) single stacking faults, and (c) stacking fault pyramids. Each of these defects is discussed in detail in the following.

A. V-shaped defect

The V-shaped defects were most common. For the sample studied in detail here, the V-shaped defect comprised $\approx 90\%$ of the total defects. Figures 3(a) and 3(b) show (100) plan-view and $(0\bar{1}1)$ cross-sectional TEM images of a single V-shaped defect, respectively. As its name suggests, the defect forms a V shape when observed in cross section. It typically consists of two pairs of dissociated dislocations which originate at the buried QD layer and then travel in opposite directions, on different $\{111\}$ planes through the GaAs capping layer to the surface. Defects with only one pair of dissociated dislocations (i.e., only one-half of the V-shaped defect) were also occasionally observed. Figure 3(c) shows a rare example of a defect where only the left side dislocation has dissociated into two partials. From plan-view images, the distance between the closely spaced dislocations is estimated to be $7 \pm 2 \text{ nm}$ which is in reasonable agreement with that determined by others for dissociated edge dislocations in GaAs.¹⁸

Figure 2 shows the V-shaped defects to have projections close to the $[011]$ and $[0\bar{1}1]$ directions when observed in (100) plan view. Therefore, the defects must lie close to the $\langle 211 \rangle$ line directions. It is also clear that the V-shaped defects show a preferred alignment along one of the $[011]$ and $[0\bar{1}1]$ directions. In this study, the crystal polarity was not determined so for simplicity the direction of preferred alignment is defined as the $[011]$ direction. This means, for instance, that in the case of a V-shaped defect with a projection along the $[011]$ direction, the left side dislocations travel on the

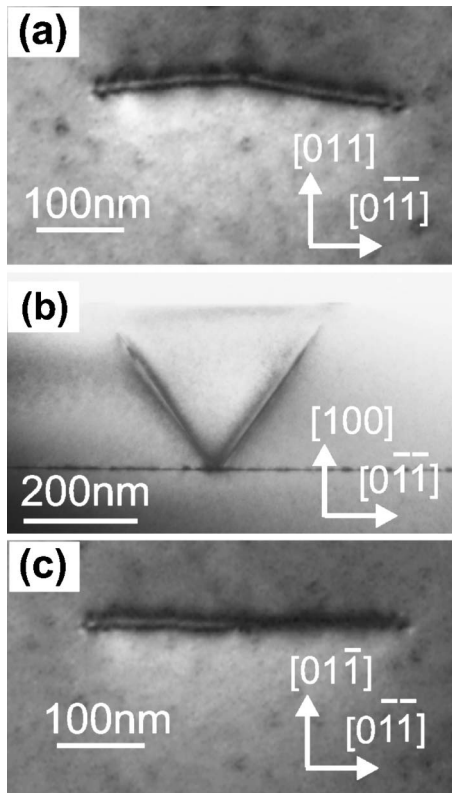


FIG. 3. Bright field TEM images of a V-shaped defect. [(a) and (c)] (100) plan view and (b) (011) cross section.

(11 $\bar{1}$) plane close to the [211] direction and the right side dislocations travel on the (111) plane close to the [2 $\bar{1}$ 1] direction.

We suspect that the preferential orientation is related to the asymmetry that exists in the GaAs zinc-blende structure and/or the type of surface reconstruction (as has been proposed to explain the asymmetry of defects in the ZnSe/GaAs system⁶). It also seems well established that defects are symmetrically injected near either end of the growing island^{2,9} which may explain the symmetric nature of the V-shaped defects with two pairs of dislocations traveling in opposite directions from the buried QD layer.

To determine the total Burgers vector \mathbf{b}_T , one of the V-shaped defects was imaged using two beam bright field conditions and different operating \mathbf{g} 's. Figure 4 shows selected images taken using the $\mathbf{g}=02\bar{2}$ and $0\bar{2}2$ reflections. The appearance of this defect is slightly different to the one shown in Fig. 3 because it is in a very thin area of the sample foil where the buried QD layer has been etched away. Therefore its middle section is missing, leaving only the segments of each dislocation pair that are located through the upper part of the GaAs capping layer. For $\mathbf{g}=02\bar{2}$ and its reverse $\mathbf{g}=0\bar{2}2$, strong contrast is observed [Figs. 4(a) and 4(b)] although it is not possible to discern each partial dislocation. In comparison, no contrast or very diffuse contrast is observed for the $\mathbf{g}=0\bar{2}\bar{2}$ and $\mathbf{g}=022$ imaging vectors, respectively [Figs. 4(c) and 4(d)]. This contrast is consistent with a total Burgers vector $\mathbf{b}_T=\pm[0\bar{1}1]$ (an edge dislocation). This can be verified with reference to Table I which summarizes the

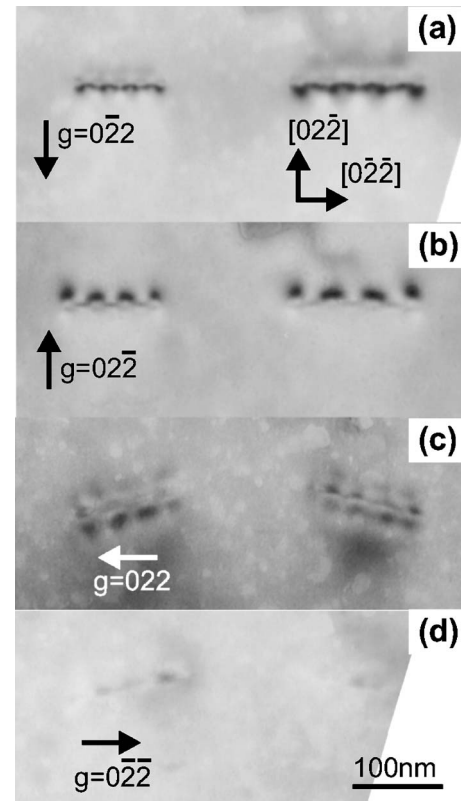


FIG. 4. Plan-view TEM images of a V-shaped defect taken under two beam bright field conditions using different imaging \mathbf{g} 's.

possible perfect and partial Burgers vectors and displacement vectors on the (111), (1 $\bar{1}$ 1), and (1 $\bar{1}$ $\bar{1}$) planes. For a total Burgers vector, $\mathbf{b}_T=\pm[0\bar{1}1]$, this table gives $|\mathbf{g}\cdot\mathbf{b}_T|=2$ and $|\mathbf{g}\cdot\mathbf{b}_T|=0$ for the 022 and $0\bar{2}2$ reflections, respectively.

Weak beam analysis was also performed on the same V-shaped defect to determine the character of each partial of the extended dislocations. Figure 5 shows weak beam images of the same V-shaped defect under different operating \mathbf{g} 's. The dissociation into two partials is clearly seen due to the much narrower image contrast. For $\mathbf{g}=02\bar{2}$, 020, and 002, both partial dislocations show strong contrast and contrast reversal under $-\mathbf{g}$ imaging [see Figs. 5(a) and 5(b) as an example]. Based on this weak beam imaging and the previous bright field analysis, the partial dislocations of the extended defects must have Burgers vectors that meet the following criteria: (1) the partials must be visible for the $\mathbf{g}=02\bar{2}$, 020, and 002 reflections and (2) the sum of the partial dislocations must add to give a total Burgers vector $\mathbf{b}_T=\pm[0\bar{1}1]$. These two conditions are satisfied by the $\frac{1}{6}\langle\bar{1}2\bar{1}\rangle$ Burgers vectors. This can be verified with reference to Table I. For example, considering the dislocation pair traveling to the right on the (111) plane, the clear visibility of both partial dislocations for $\mathbf{g}=02\bar{2}$ eliminates the $\pm\frac{1}{6}[2\bar{1}\bar{1}]$ Burgers vector. We therefore attribute the $\pm\frac{1}{6}[\bar{1}2\bar{1}]$ Burgers vector to one of the partials and the $\pm\frac{1}{6}[\bar{1}\bar{1}2]$ Burgers vector to the other such that they add to give a total Burgers vector $\pm\mathbf{b}_T=\frac{1}{2}[0\bar{1}1]$. A similar analysis of the dislocation pair trav-

TABLE I. $\mathbf{g} \cdot \mathbf{b}$ values for different reflections on the $[100]$ zone axis.

Plane	\mathbf{b}	\mathbf{g}			
		022	020	002	$0\bar{2}\bar{2}$
(111)	$\frac{1}{2}[10\bar{1}]$	-1	0	-1	1
	$\frac{1}{2}[0\bar{1}1]$	0	-1	1	-2
	$\frac{1}{2}[\bar{1}10]$	1	1	0	1
	$\frac{1}{6}[\bar{1}2\bar{1}]$	$\frac{1}{3}$	$\frac{2}{3}$	$-\frac{1}{3}$	1
	$\frac{1}{6}[\bar{1}\bar{1}2]$	$\frac{1}{3}$	$-\frac{1}{3}$	$\frac{2}{3}$	-1
	$\frac{1}{6}[2\bar{1}\bar{1}]$	$-\frac{2}{3}$	$-\frac{1}{3}$	$-\frac{1}{3}$	0
	$\frac{1}{3}[111]$	$-\frac{4}{3}$	$-\frac{2}{3}$	$-\frac{2}{3}$	0
$(\bar{1}\bar{1}1)$	$\frac{1}{2}[011]$	2	1	1	0
	$\frac{1}{2}[\bar{1}\bar{1}0]$	-1	-1	0	-1
	$\frac{1}{2}[\bar{1}0\bar{1}]$	-1	0	-1	1
	$\frac{1}{6}[112]$	1	$\frac{1}{3}$	$\frac{2}{3}$	$-\frac{1}{3}$
	$\frac{1}{6}[\bar{1}2\bar{1}]$	-1	$-\frac{2}{3}$	$-\frac{1}{3}$	$-\frac{1}{3}$
	$\frac{1}{6}[\bar{2}1\bar{1}]$	0	$\frac{1}{3}$	$-\frac{1}{3}$	$\frac{2}{3}$
	$\frac{1}{3}[\bar{1}\bar{1}1]$	0	$-\frac{2}{3}$	$\frac{2}{3}$	$-\frac{4}{3}$
$(1\bar{1}\bar{1})$	$\frac{1}{2}[\bar{1}\bar{1}0]$	-1	-1	0	-1
	$\frac{1}{2}[101]$	1	0	1	-1
	$\frac{1}{2}[01\bar{1}]$	0	1	-1	2
	$\frac{1}{6}[\bar{1}\bar{1}2]$	$-\frac{1}{3}$	$\frac{1}{3}$	$-\frac{2}{3}$	1
	$\frac{1}{6}[\bar{1}2\bar{1}]$	$-\frac{1}{3}$	$-\frac{2}{3}$	$\frac{1}{3}$	-1
	$\frac{1}{6}[211]$	$\frac{2}{3}$	$\frac{1}{3}$	$\frac{1}{3}$	0
	$\frac{1}{3}[1\bar{1}\bar{1}]$	$-\frac{4}{3}$	$-\frac{2}{3}$	$-\frac{2}{3}$	0

eling to the left on the $(1\bar{1}\bar{1})$ plane with a $[211]$ line direction gives partial dislocations with Burgers vectors $\pm\frac{1}{6}[\bar{1}2\bar{1}]$ and $\pm\frac{1}{6}[1\bar{1}2]$.

Up to now we have ignored the $\mathbf{g}=\pm 022$ weak beam image shown in Fig. 5(c). The weak beam contrast observed for this reflection is not as easily interpreted and does not show a clear separation of the partial dislocations under either \mathbf{g} or $-\mathbf{g}$ imaging. It is therefore not obvious if it corresponds to two indistinguishable partials and/or to a stacking fault. However, according to our above Burgers vector assignments, the partials should be visible under this reflection. For the $\mathbf{g}=022$ reflection, $\mathbf{g} \cdot \mathbf{b}=0$ for the extended defect, and may cause the ambiguous weak beam contrast.

B. Single stacking faults

The second type of defect is shown in Fig. 6(a) and was only ever observed in the direction orthogonal to that preferred by the V-shaped defects. It was extremely rare, comprising only 2% of the defects for the sample reported here.¹⁹ Again it consists of a dissociated pair of dislocations; however, these are spaced further apart (≈ 50 nm) with a stacking fault in between. One striking feature of the single stacking faults is that they often originated from very large relaxed islands which exhibited clear moiré fringes, as seen in Fig. 6(a).

Figures 6(b)–6(e) show a series of weak beam images of a similar defect using different \mathbf{g} 's. This defect is again in a very thin region of the foil where the buried QD layer has

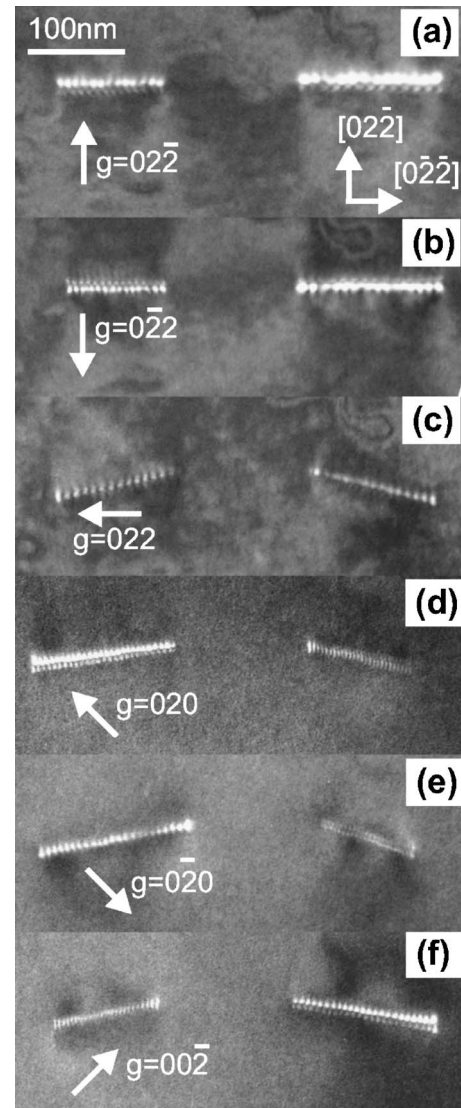


FIG. 5. Weak beam, plan-view TEM images of a V-shaped defect taken under different imaging \mathbf{g} conditions. The defect is in a thin region of the foil where the buried QD layer has been etched away.

been etched away. However, trace analysis of this defect shows that it has a $(\bar{1}\bar{1}1)$ habit plane and a $[2\bar{1}1]$ line direction. The bounding dislocations are visible in all four reflections while the stacking fault fringes are visible for all reflections except for $\mathbf{g}=\pm 022$. According to the $\mathbf{g} \cdot \mathbf{b}=0$ criterion, the diffraction contrast is consistent with Shockley-type bounding dislocations with $\mathbf{b}=\pm\frac{1}{6}[112]$ and $\pm\frac{1}{6}[\bar{1}2\bar{1}]$ and can be confirmed with reference to Table I.

There are four possible combinations of Burgers vectors that the two dislocation partials may have with respect to each other: (a) the same Burgers vector, (b) opposite Burgers vector dipoles, (c) two types of Burgers vectors (e.g., $\mathbf{b}_1=\frac{1}{6}[112]$ and $\mathbf{b}_2=\frac{1}{6}[\bar{1}2\bar{1}]$) that originated from a screw dislocation with $\mathbf{b}_T=\frac{1}{6}[2\bar{1}1]$, and finally (d) two types of Burgers vectors (e.g., $\mathbf{b}_1=\frac{1}{6}[112]$ and $\mathbf{b}_2=\frac{1}{6}[\bar{1}2\bar{1}]$) that originated from an edge dislocation with $\mathbf{b}_T=\frac{1}{2}[011]$. The change in separation of the two partials with \mathbf{g} and $-\mathbf{g}$ imaging (i.e., inside/outside contrast) can give an indication of the sign of the Burgers vector of the defect.¹⁷ We note that the two par-

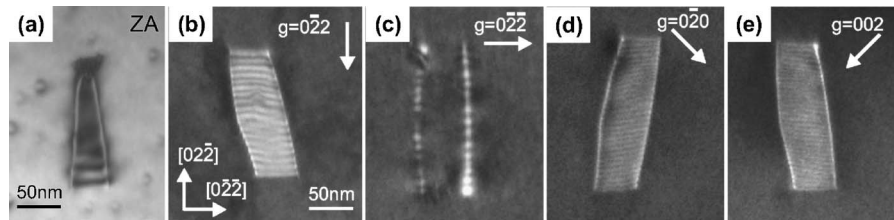


FIG. 6. Plan-view TEM images of the second type of defect. (a) is a $[100]$ on-axis bright field image. Due to the rarity of this defect, image (a) is taken from a second sample in which the QDs were deposited directly onto GaAs (no InGaAs buffer layer) with a deposition rate of 0.25 ML/s and a coverage of 2 ML. All other growth conditions are identical to those described in the Experiment section. For this sample more of the capping layer was etched prior to TEM sample preparation making the defect appear shorter. (b)–(e) are weak beam images taken under different imaging \mathbf{g} conditions. The defect shown in (b)–(e) is in a thin region of the foil where the QD layer has been etched away.

tials show a change in separation when imaged using $\mathbf{g} = \pm 02\bar{2}, \pm 020, \pm 002$, but no change in the separation when imaged using $\mathbf{g} = \pm 022$. This inside/outside contrast can only be explained for all \mathbf{g} reflections by the combination (d) where the Burgers vector of the individual Shockley partials add up to an edge dislocation with $\mathbf{b}_T = \pm \frac{1}{2}[011]$. Surprisingly this is identical to that determined for the V-shaped defects which were also occasionally observed aligned in the same $[0\bar{1}1]$ orientation as the single stacking faults, yet the two types of defects show very different spacing between the bounding partial dislocations. The larger relaxed islands from which the single stacking faults originate may be connected with their larger stacking fault area.

Another possibility is the Frank Burgers vector, $\mathbf{b} = \pm \frac{1}{3}[\bar{1}\bar{1}1]$. However, while this satisfies the visibility criteria,²⁰ it cannot explain the inside/outside contrast observed for $\mathbf{g} = \pm[022]$.

C. Stacking fault pyramids

Both complete stacking fault pyramids [see Fig. 7(a)] and incomplete stacking fault pyramids (see Fig. 10) were observed and comprised $\approx 8\%$ of the total defects. They consist of $\{111\}$ stacking faults which originate at the buried QD layer and then travel through the GaAs capping layer to intersect the sample surface in a square along the $[0\bar{1}\bar{1}]$ and $[0\bar{1}1]$ directions. Figure 8(a) shows a three-dimensional schematic of a stacking fault pyramid while Fig. 8(b) shows the important crystallographic directions as projected on the (100) plane.

Weak beam images of a complete stacking fault pyramid using different diffraction vectors are shown in Fig. 7. In some cases, the dislocations showed strong contrast under \mathbf{g} but little or no contrast under the reverse \mathbf{g} . For example, dislocation 1 disappears in Fig. 7(b) for $\mathbf{g} = 0\bar{2}2$ but is clearly visible in Fig. 7(c) for $\mathbf{g} = 02\bar{2}$. True invisibility is defined when the defects are not observed for both $\pm\mathbf{g}$ and therefore these dislocations are assumed to be visible. Using this criterion, the bounding dislocations [labeled 1 and 3 in Fig. 7(a)] along the $[110]$ and $[1\bar{1}0]$ directions are visible when imaged using all the \mathbf{g} reflections except for $\mathbf{g} = \pm 020$, while the bounding dislocations (labeled 2 and 4) along the $[10\bar{1}]$ and $[101]$ directions are visible for all imaging \mathbf{g} except for $\mathbf{g} = \pm 002$. In order to satisfy both the $\mathbf{g} \cdot \mathbf{b}$ and $\mathbf{g} \cdot (\mathbf{b} \times \mathbf{u})$ criteria, dislocations 1 and 3 have only three possible Burgers

vectors, namely, $\pm \frac{1}{3}[001]$, $\pm \frac{1}{6}[301]$, and $\pm \frac{1}{6}[\bar{3}01]$. Likewise dislocations 2 and 4 have only three possible Burgers vectors, $\pm \frac{1}{3}[010]$, $\pm \frac{1}{6}[310]$, and $\pm \frac{1}{6}[3\bar{1}0]$. This can be confirmed for the third and fourth dislocations with reference to Table II. Similar stacking fault pyramids have been observed in the ZnSe/GaAs system where the bounding dislocations were also identified as stair-rod type.⁵

Clear extinction of the stacking faults is also observed in Figs. 7(b)–7(d). The stacking fault contrast on the (111) and $(\bar{1}\bar{1}1)$ planes disappears for a $\mathbf{g} = 0\bar{2}2$ imaging vector, while the orthogonal imaging vector, $\mathbf{g} = 022$, leads to extinction of the stacking fault contrast on the $(\bar{1}\bar{1}1)$ and $(\bar{1}\bar{1}\bar{1})$ planes. However, this stacking fault contrast cannot distinguish between a Frank or Shockley partial (see Table I). Due to the

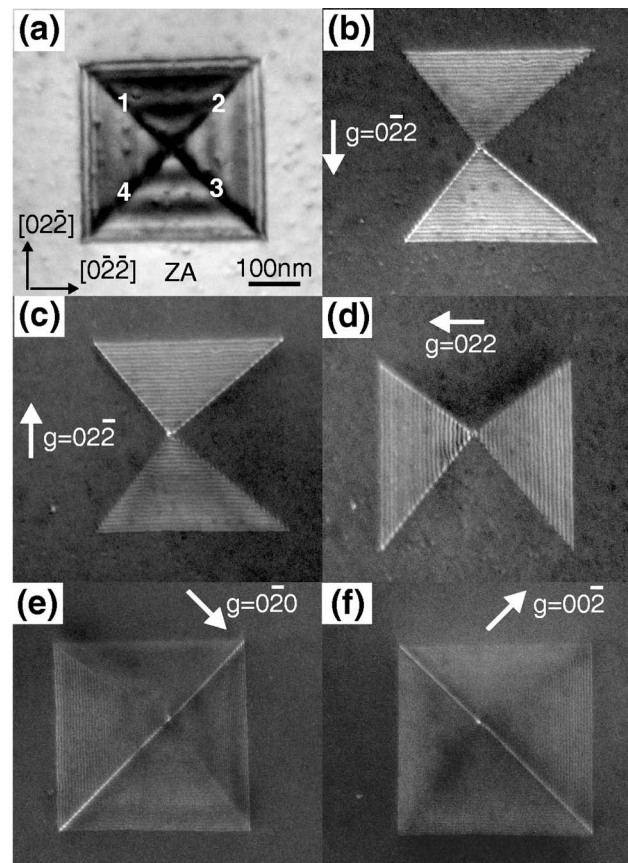


FIG. 7. Plan-view TEM images of a complete stacking fault pyramid. (a) $[100]$ on-axis bright field image. [(b)–(f)] weak beam images under different imaging \mathbf{g} conditions.

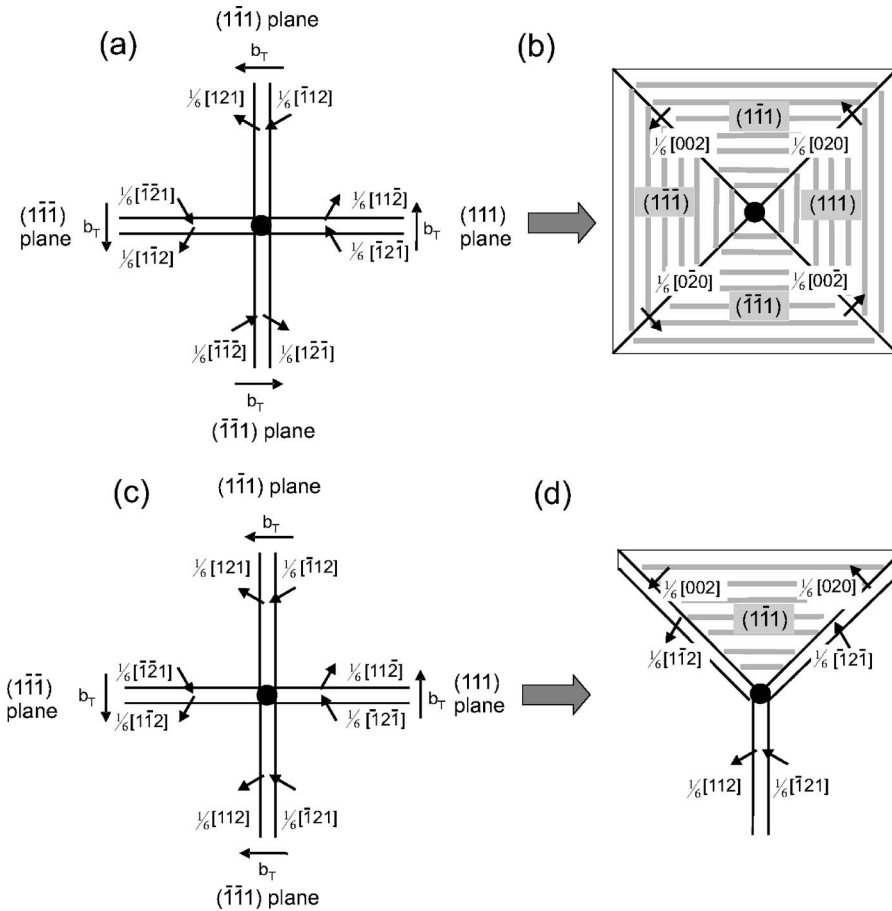


FIG. 9. Possible formation mechanism of [(a) and (b)] a complete stacking fault pyramid and [(c) and (d)] an incomplete stacking fault pyramid.

shown in Fig. 9(b). The partials interact to form bounding stair-rod dislocations with $\mathbf{b} = \frac{1}{6}\langle 002 \rangle$ according to the reaction,

$$\frac{1}{6}[\bar{1}2\bar{1}](111) + \frac{1}{6}[\bar{1}2\bar{1}](\bar{1}\bar{1}\bar{1}) \rightarrow \frac{1}{6}[00\bar{2}]. \quad (1)$$

This represents a significant reduction in energy when applying Frank's rule,²²

$$\frac{a^2}{6} + \frac{a^2}{6} \rightarrow \frac{a^2}{9}. \quad (2)$$

The $\mathbf{b} = \frac{1}{6}\langle 002 \rangle$ stair-rod dislocation is also one of the possible Burgers vectors determined from our diffraction analysis of the stacking fault pyramid.

The model is also able to account for incomplete stacking fault pyramids. These form when the arrangement of the Shockley partials makes it energetically unfavorable for some of the pairs to split apart and interact. The exact configuration of the incomplete pyramid depends on the initial arrangement of the Shockley partials. Figures 9(c) and 9(d) illustrate a second scenario which leads to the formation of an incomplete pyramid which closely resembles the one shown in Fig. 10(a). The main difference between this scenario and the previous one is that the two dissociated partial dislocations on the $(\bar{1}\bar{1}\bar{1})$ plane have been reversed. This means that the dissociated partials on adjacent $\{111\}$ planes in the lower part of the pyramid figure are now repulsive. In this case, the dissociated dislocation pair traveling along the

$[2\bar{1}1]$ direction on the $(\bar{1}\bar{1}\bar{1})$ plane remains unchanged and stair-rod formation is only favorable along the $[10\bar{1}]$ and $[110]$ directions. This leaves a single unreacted partial dislocation on each of the (111) and $(\bar{1}\bar{1}\bar{1})$ planes. These two unreacted dislocations are expected to remain close to the stair-rod dislocations in order to minimize the energy associated with the stacking fault. This is further supported by evidence of stacking fault fringes between two dislocations bounding the edge of the incomplete pyramid, as shown in Fig. 10(b). Clearly this model accounts well for both complete and incomplete stacking fault pyramid formations.

This model also seems to be in agreement with the TEM analysis of Ref. 5 in which similar incomplete stacking fault pyramids were observed for the ZnSe/GaAs system. Their analysis of an incomplete pyramid identified the closed boundaries as stair-rod dislocations and the open boundaries as 30° Shockley partials, in agreement with our model. It is also worth noting that the incomplete stacking fault pyramids in Ref. 5 have a slightly different configuration to ours due to a preference for the Shockley partial pairs to separate and travel along the $\langle 101 \rangle$ directions, revealing triangular stacking faults in between them. This leads, for example, to opposing pairs of triangular stacking faults instead of our V-shaped defects. This difference is likely due to the larger GaAs stacking fault energy compared to ZnSe (45 ± 7 vs 13 ± 1 mJ/m²) (Ref. 23) as well as the thicker capping layer used by us.²⁴

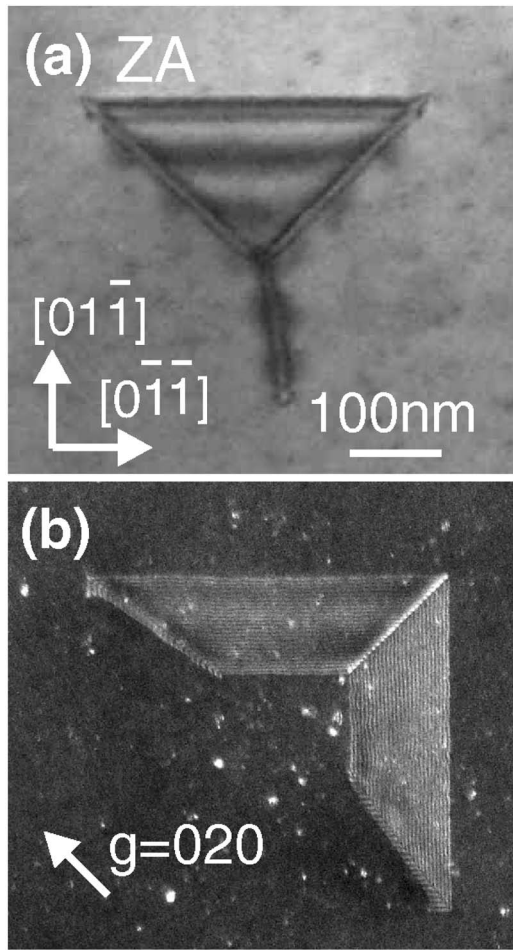


FIG. 10. (a) A bright field, plan-view image of single sided pyramid. (b) A weak beam image of another incomplete stacking fault pyramid with $g=020$. This pyramid is in a thin region of the foil where the QD layer has been etched away giving it a truncated appearance. The stacking fault between the two pairs of closely spaced dislocations can be clearly seen.

V. CONCLUSIONS

Both plan-view and cross-sectional transmission electron microscopy have been used to study the main defects formed during self-assembled growth and capping of InAs/GaAs QDs. Three main defect types were identified, namely, V-shaped defects, single stacking faults, and stacking fault pyramids. The V-shaped defects were by far the most common comprising 90% of the total defects. They were identified to consist of pairs of 60° Shockley partials originating from an edge-type dislocation. The type of bounding partials for the single stacking faults is not as clear. An initial analysis seems to suggest that they also consist of 60° Shockley partials. However, the wider separation of the partials and increased stacking fault area are surprising and may be related

to the very large relaxed islands from which they often originated. Both complete and incomplete stacking fault pyramids were observed. In the case of the complete stacking fault pyramid, the bounding dislocations along the $[110]$, $[1\bar{1}0]$, $[10\bar{1}]$, and $[101]$ directions were identified as stair rods. A possible mechanism for the stacking fault pyramid formation, which can also account for the creation of incomplete stacking fault pyramids, was also presented.

ACKNOWLEDGMENTS

We acknowledge the expert advice of Dr. Vince Craig and Dr. John Fitz Gerald for work with the AFM and TEM instruments, respectively. We also acknowledge the financial support of the Australian Research Council.

- ¹A. Saka and T. Tatsumi, Phys. Rev. Lett. **71**, 4007 (1993).
- ²S. Guha, A. Madhukar, and K. C. Rajkumar, Appl. Phys. Lett. **57**, 2110 (1990).
- ³B. J. Spencer and J. Tersoff, Appl. Phys. Lett. **77**, 2533 (2000).
- ⁴S. N. G. Chu, W. T. Tsang, T. H. Chiu, and A. T. Macrander, J. Appl. Phys. **66**, 520 (1989).
- ⁵N. Wang, I. K. Sou, and K. K. Fung, J. Appl. Phys. **80**, 5506 (1996).
- ⁶Y. Ohno, N. Adachi, and S. Takeda, Appl. Phys. Lett. **83**, 54 (2003).
- ⁷N. Wang, K. K. Fung, and I. K. Sou, Appl. Phys. Lett. **77**, 2846 (2000).
- ⁸L. H. Kuo, L. Salamanca-Riba, B. J. Wu, G. M. Haugen, J. M. DePuydt, G. Hofer, and H. Cheng, J. Vac. Sci. Technol. B **13**, 1694 (1995).
- ⁹N. Y. Jin-Phillipp and F. Phillipp, J. Microsc. **194**, 161 (1999).
- ¹⁰Y. Chen, X. W. Lin, Z. Liliental-Weber, J. Washburn, J. F. Klem, and J. Y. Tsao, Appl. Phys. Lett. **68**, 111 (1996).
- ¹¹O. Ueda, Y. Nakata, and S. Muto, *Tenth International Conference on Indium Phosphide and Related Materials* (IEEE, Piscataway, NJ, 1998), p. 773.
- ¹²K. Shiramine, Y. Horisaki, D. Suzuki, S. Itoh, Y. Ebiko, S. Muto, Y. Nakata, and N. Yokoyama, J. Cryst. Growth **205**, 461 (1999).
- ¹³K. Stewart, J. Wong-Leung, H. H. Tan, and C. Jagadish, J. Appl. Phys. **94**, 5283 (2003).
- ¹⁴K. Sears, H. H. Tan, J. Wong-Leung, and C. Jagadish, J. Appl. Phys. **99**, 044908 (2006).
- ¹⁵K. Sears, J. Wong-Leung, H. H. Tan, and C. Jagadish, J. Cryst. Growth **281**, 290 (2005).
- ¹⁶K. Sears, J. Wong-Leung, M. Buda, H. H. Tan, and C. Jagadish, *Proceedings: Conference on Optoelectronic and Microelectronic Materials and Devices* (IEEE, Piscataway, NJ, 2004), pp. 1–4.
- ¹⁷D. B. Williams and C. B. Carter, *Transmission Electron Microscopy: Part III: Imaging*, 1st ed. (Plenum Corporation, New York, 1996).
- ¹⁸H. Gottschalk, G. Patzer, and H. Alexander, Phys. Status Solidi A **45**, 207 (1978).
- ¹⁹Single stacking faults were slightly more common, comprising up to 25% of the total defects for other samples in which the growth conditions led to larger island sizes.
- ²⁰While the $g \cdot b$ component is zero for the $g=022$ reflection (Table I), the $g \cdot (b \times u)$ component is substantial (equal to 1.6).
- ²¹J. P. Hirth and J. Lothe, *Theory of Dislocations*, 2nd ed (Wiley, New York, 1982).
- ²²D. Hull and D. J. Bacon, *Introduction to Dislocations*, 4th ed. (Butterworth Heinemann, Oxford, 2001).
- ²³S. Takeuchi and K. Suzuki, Phys. Status Solidi A **171**, 99 (1999).
- ²⁴H. Heun, J. J. Paggel, L. Sorba, S. Rubini, A. Franciosi, J.-M. Bonard, and J.-D. Ganière, Appl. Phys. Lett. **70**, 237 (1996).